Microfluidics and Nanofluidics (2024) 28:35
https://doi.org/10.1007/s10404-024-02734-y

RESEARCH

Design and proof-of-concept of a micropillar-based microfluidic chip for trapping and culture of single cells

Thu Hang Nguyen[1] · Ngoc Anh Nguyen Thi[2] · Hang Bui Thu[1,3] · Tung Thanh Bui[1] · Trinh Chu Duc[1] · Loc Do Quang[2]

Received: 27 January 2024 / Accepted: 29 April 2024 / Published online: 9 May 2024

Abstract

Single-cell analysis provides a groundbreaking avenue for exploring cell-to-cell variation, the heterogeneity of cell responses to stimuli, and the impact of DNA sequence variations on cell phenotypes. A crucial facet of this analytical approach involves the refinement of techniques for effective single-cell trapping and sustained culture. This study introduces a microfluidic platform based on micropillars for hydrodynamic trapping and prolonged cultivation of individual cells. The proposed biochip design, termed three-micropillars based microfluidic (3μPF) structure, incorporates interleaved trap units, each featuring three-micropillars based microfluidic structure strategically designated to trap single cells, enhance the surface area of cells exposed to the culture medium, and enable dynamic culture, continuous waste removal. This configuration aims to mitigate adverse effects associated with bioparticle collisions compared to conventional trap units. The study employs finite element method to conduct a comprehensive numerical investigation into the operational mechanism of the microfluidic device. The simulation results show that the filled trap unit demonstrates a low-velocity magnitude, reducing shear stress on cells and facilitating extended culture. The hydrodynamic single-cell trap mechanism of the proposed device was also verified. The insights derived from this work are pivotal for optimizing the device and guiding future experimental examinations, thus contributing significantly to the progression of single-cell analysis techniques.

Keywords Single-cell trapping · Microfluidic · Micropillar · Long-term cell culture · Single-cell analysis

1 Introduction

Recent years have witnessed the impressive development of microfluidic technology (Aubry et al. 2023). Microfluidics refers to a system that manipulates small amounts of liquid at micro and nanometer scales using channels ranging in size from ten to several hundred micrometers (Zhang et al. 2023). Microfluidic technique has found diverse applications across various fields of research and industry, including material synthesis and discovery, automated systems, lab-on-a-chip and point-of-care (PoC) devices, and biosensors (Jiang and Korivi 2014). Microfluidic technology is a promising tool for biomedicine applications, especially for single-cell trapping and analysis (Zhou et al. 2021). Single-cell trapping can be defined as the process of immobilizing single cells in devices for further manipulation and analysis. Single-cell trapping techniques offer precise control, enhanced sensitivity, and valuable insights into cellular functions (Sinha et al. 2022). Their ability to focus on individual cells reveals hidden nuances in cellular responses and allows for a thorough exploration of heterogeneity within populations. The single-cell analysis offers a novel approach to study individual cells, the differences in cell responses, and the genetic heterogeneity based on single-cell DNA or RNA sequence analysis (Bakker et al. 2016; Goldman et al. 2019; Muhl et al. 2020). Integrated into advanced platforms, these techniques can be applied in versatile applications across scientific disciplines, from genomics to drug discovery and cancer research (Wen et al. 2022; Van de Sande et al. 2023). Microfluidic devices offer

✉ Loc Do Quang
locdq@vnu.edu.vn

[1] University of Engineering and Technology, Vietnam National University, Hanoi, Vietnam

[2] University of Science, Vietnam National University, Hanoi, Vietnam

[3] Faculty of Mathematics and Computer Science, Babes-Bolyai University, Cluj-Napoca, Romania

several advantages over conventional methods for single-cell trapping and analysis, such as low sample consumption, high spatial and temporal resolution, multiplexing capability, and integration with other analytical techniques (Yin and Marshall 2012; Dusny and Grünberger 2020).

Not only in single-cell research, microfluidics finds extensive application in cell culture for increasing our understanding of cell study, tissue morphology, pathology, drug release and their effects, protein production (Kapałczyńska et al. 2016). Cell culture on a chip is a technique that allows researchers to study cells in a more controlled environment. Microfluidic devices can also create dynamic microenvironments that can mimic physiological conditions or induce cellular responses (Xu et al. 2020; Dusny and Grünberger 2020). The use of cell culture chips presents a significant advantage over traditional culture methods, such as batch culture or dynamic cell culture. The dynamic microenvironments achieved through microfluidic systems allow for more intricate control and modulation of the culture conditions, facilitating the emulation of in vivo-like scenarios. This dynamic control is particularly beneficial for mimicking complex cellular interactions, inducing cell differentiation, and simulating various physiological cues (Kim and Hayward 2012). In essence, cell culture on a chip offers a superior and more versatile platform for studying cells under conditions that closely mirror their natural milieu, providing a valuable tool for advancing our understanding of cellular behavior and responses.

In recent years, the trapping and cultivation of single cells using microfluidic chips have attracted considerable attention from many research groups. Jo et al. designed a single-cell analysis platform based on the microfluidic chip to investigate the replicative aging phenomenon in the budding yeast *Saccharomyces cerevisiae* (Jo et al. 2015a). The biochip contained an array of U-shaped single-cell trapping units in the chamber. The proposed design efficiently trapped up to 8,000 single yeast cells with a trapping efficiency of 96% and enabled long-term culture of trapped cells. Xu et al. designed, numerically examined, and optimized the microfluidic chip for single-cell trapping with inverted trapezoidal trap grooves (Xu et al. 2013a, b). A recent work presented a microfluidic chip for separating plasma, red blood cells, and individual trapping of white blood cells (Kuan et al. 2018). The trapping structure consisted of a triangular pillar and two rectangular pillars, which allowed trapping up to approximately 1800 cells in 20 min. However, the U-shaped trap structure in long-term cell culture presents challenges due to the limited contact area between the cell and the culture media when cells are trapped within the trap units, which could potentially impede the exchange between the culture medium and the cell surface. In case of inverted trapezoidal grooves or triangular pillars, the presence of corners may result in cell damage due to collisions during the trapping process (Xu et al. 2013a). During the cultivation phase, it can lead to deformations and potential harm to the cells. To address the aforementioned limitations, a new structure has been proposed for both cell trapping and long-term dynamic culture while minimizing cell damage.

This study proposes a micropillar-based microfluidic platform for both hydrodynamic trapping and long-term dynamic culture of single cells, which could be integrated into other platforms such as biosensors and real-time microscopy. The three-micropillars based microfluidic (3μPF) structure features interleaved trap units for hydrodynamic cell trapping. Each trap unit was designated with three well-aligned micropillars to enhance the surface area of single-cell exposed to the culture medium and reduce the negative effects when the bioparticles collide with the trap. In this work, the finite element method (FEM) was used to analyze the working principle of the microfluidic device and optimize the biochip structure. The simulation results showed that the proposed design enables trapping and long-term culture of single cells.

2 Theoretical fundamentals

The operating principle of the 3μPF was examined through numerical computations using COMSOL Multiphysics 6.0 software. In this study, the fluid flow was considered a creeping flow, calculated by the Navier-Stokes equations, while the simulated cell follow the linear elastic dynamics and Newton's equation of motion. The cell movements are governed by the combination of liquid and solid mechanics, or fluid-solid interaction (FSI). The fundamental concept is that a structural component experiences hydrodynamic forces exerted by a fluid, leading to its subsequent deformation (Peksen 2018). In turn, the deformed shape of the structure imparts velocity to the fluid domain, inducing changes in the flow field. The continual motion and interactions of both the fluid and particles lead to a deformation of the mesh geometry. To capture this dynamic behavior, the Arbitrary Lagrangian-Eulerian (ALE) technique is employed. This technique effectively characterizes the dynamics associated with the deforming geometry and the moving boundaries of the mesh. Its application facilitates the generation of a new mesh, ensuring the preservation of numerical stability and accuracy throughout the computational process (Xu et al. 2013a; Abbas et al. 2022).

2.1 Fluid flow

The fluid flow behaviours are governed by the incompressible Navier-Stokes equations, as shown in Eqs. (1), (2) (Henrik Bruus 2008):

$$\rho[\frac{\partial \boldsymbol{u_f}}{\partial \boldsymbol{t}} + \boldsymbol{u_f}.\nabla \boldsymbol{u_f}] = \nabla.[-\boldsymbol{pI} + \boldsymbol{K}] - 12\frac{\boldsymbol{\mu u_f}}{\boldsymbol{d_z^2}} + F \tag{1}$$

$$\rho \nabla \cdot \boldsymbol{u}_f = 0 \tag{2}$$

where $_{\rho}$,$\boldsymbol{u}_f = (\boldsymbol{u}_f, v_f, w_f) = 0$,t, $_{p,}\boldsymbol{I}$, and $\boldsymbol{F}$ are the fluid density (kg/m^3), the fluid velocity field (m/s, m/s, m/s), the time (s), the pressure (Pa), the identity matrix, is the volume force affecting the fluid (N/m^3, or N/m^2 for a 2D model), respectively. For a pressure-driven flow without gravitation or other volume forces, $F = 0$. Moreover, $\rho\frac{\partial \boldsymbol{u}_f}{\partial t}$ represents the unsteady inertia force (N/m^3). The fluid is assumed Newtonian with the corresponding constitutive equation is written by:

$$K = \mu\left(\nabla_{\boldsymbol{u}_f} + (\nabla \boldsymbol{u}_f)^T\right) \tag{3}$$

where T indicates the transposition, K refers to the shear stress tensor, μ is the fluid dynamic viscosity ($Pa.s$).

In this study, 2D simulation models were implemented to simplify the computations and reduce time and resources due to the model symmetry. In microfluidic channels characterized by an approximately rectangular cross-section, where the thickness is considerably smaller than the channel width, basic 2D models often prove inadequate in yielding precise results. This inadequacy arises from the omission of boundaries in these models, a critical factor that significantly influences the flow dynamics (Xu et al. 2013a). To account for the influence of these boundaries, a shallow channel approximation is introduced (Henrik Bruus 2008). This approximation introduces a drag term as a volumetric force in the fluid flow equation. This term signifies the resistance exerted by the parallel boundaries on the flow. In other words, Eq. (1) is an equation from COMSOL Multiphysics that has been adjusted to give a more accurate calculation result. The drag term is calculated by the following equation (Xu et al. 2013a):

$$F_{\mu} = -12\frac{\mu \boldsymbol{u}_f}{d_z^2} \tag{4}$$

where d_z is the channel thickness (m).

The dimensionless number used to define the ratio of the advective to viscous forces is known as Reynolds number, Re. Reynolds number is given by the following relation:

$$Re = \frac{\rho UL}{\mu} \tag{5}$$

where U is the velocity of the fluid (m/s), L is the characteristic length of the fluid (m).

In case of flow in microfluidics devices, Re becomes very low (Re $<<$ 1). The Strouhal number $S_{tr} = \frac{fL}{U}$ (f is the frequency of vortex shedding) is significant (on the order of 1), and viscosity plays a dominant role in governing the fluid flow, it leads to a collective oscillating motion of the fluid. In this work, the fluid flow is Stokes flow, commonly referred to as creeping flow or creeping motion. Stokes flow represents a type of fluid motion wherein advective inertial forces are notably smaller compared to viscous forces. Therefore, the non-linear inertial force $\rho(\boldsymbol{u}_f.\nabla)\boldsymbol{u}_f$ can be neglected.

2.2 Solid mechanics

Solid mechanics is a pivotal discipline in physical science which focuses on the deformation and movement of continuous solids subjected to external forces such as forces, displacements, and accelerations (Wang and Qin 2019). In the case of our solid subject to small deformation and low load, it will have isotropic linear elasticity. By conceptualizing cells as solid structures, this work accurately models and simulates their mechanical traits, including elasticity and deformability. Employing solid mechanics principles facilitates an accurate representation of cellular responses to external forces, deformation under mechanical stress, and interactions within their immediate surroundings. Utilizing FEM to simulate the solid phase in FSI models allows for the intricate modeling of individual cell mechanics, providing nuanced insights into their behavior across diverse fluidic environments. This method harmonizes biological understanding with classical solid mechanics, enhancing the computational representation of cellular dynamics for academic and research purposes. The solid's displacement and deformation follow the governing equations of linear elastodynamics (Bower 2009):

$$\epsilon_s = \frac{1}{2}\left[(\nabla \boldsymbol{u}_s)^T + \nabla \boldsymbol{u}_s + (\nabla \boldsymbol{u}_s)^T(\nabla \boldsymbol{u}_s)\right], \tag{6}$$

$$\nabla_{\boldsymbol{\sigma}_s} + \boldsymbol{F}_s = \rho_s\frac{\partial^2_{\boldsymbol{u_s}}}{\partial_t^2}, \tag{7}$$

$$\boldsymbol{\sigma}_s = C\epsilon_s. \tag{8}$$

Here, Eq. (6) is the strain-displacement (compatibility) equation, with $_{\epsilon_s}$ denoting the infinitesimal strain tensor and $\boldsymbol{u}_s = (\boldsymbol{u}_s, v_s, w_s)$ denoting the solid displacement field (m, m, m).

Equation (7) is Newton's equation of motion, with $\boldsymbol{\sigma}_s$ the Cauchy stress tensor, $\boldsymbol{F}_s$ is the body force per unit volume (N/m^3) or boundary force per unit area in 2D (N/m^2), and ρ_s denoting the solid density (kg/m^3).

The stress-strain relations for an isotropic, linear elastic solid are repeated below for convenience. Equation (7) is the linear elastic stress-strain law with $\mathrm{C} = \mathrm{C}(\mathrm{E}, \nu)$ as the stiffness matrix given by

$$C = \frac{E}{(1+v)(1-2v)} \begin{bmatrix} 1-v & v & v & 0 & 0 & 0 \\ v & 1-v & v & 0 & 0 & 0 \\ v & v & 1-v & 0 & 0 & 0 \\ 0 & 0 & 0 & 1-2v & 0 & 0 \\ 0 & 0 & 0 & 0 & 1-2v & 0 \\ 0 & 0 & 0 & 0 & 0 & 1-2v \end{bmatrix} \tag{9}$$

Here, E and v are Young's modulus (Pa) and Poisson's ratio of the solid.

2.3 Fluid-solid interaction (FSI)

Fluid–solid interaction (FSI) applications involve the coupling of fluid dynamics and structural mechanics disciplines, in general. The interaction equations are determined through:

$$\boldsymbol{F}_A = [-\rho \boldsymbol{I} + K] \cdot n \tag{10}$$

$$\boldsymbol{u}_{tr} = \frac{\partial_{\boldsymbol{u}_s}}{\partial_t} \tag{11}$$

In this, $\boldsymbol{F}_A$ represents the total force (caused by the fluid pressure and viscous force) exerted on the solid boundary, K is presented in the Eq. (3) and $\boldsymbol{n}$ is the outward normal to the boundary. From Eq. (11), $\boldsymbol{u}_{tr}$ is the rate of change for the displacement of the solid. In this case, $\boldsymbol{u}_{tr}$ equal to the fluid velocity $\boldsymbol{u}_f$. In other words, at the liquid-solid interface, a non-slip boundary condition is formed for the liquid domain.

3 Design and setup of numerical simulation

3.1 Design of the microfluidic single-cell trapping device

Figure 1 illustrates the proposed 3 $_\mu$PF design with interleaved trap units. The microfluidic channel presented in this report is designed with two inlets and one outlet. Experimentally, micropillars within each trap units can be potentially made of polydimethylsiloxane (PDMS), with each trap unit designated with three micropillars to enhance the surface area of single-cell exposed to the culture medium and reduce the negative effects when the bioparticles collide with the trap, which helps overcome the limitations of other trap unit designs (Xu et al. 2013a; Jo et al. 2015b) (Fig. 1).

Hydrodynamic trapping employs mechanical barriers or obstructions to segregate the target particle from the main flow. Once separated, these target particles are captured and held in hydrodynamic trapping sites, facilitating their utilization for various investigative purposes (Narayanamurthy et al. 2017). Our 3 $_\mu$PF, constructed from precisely aligned micropillars, enable hydrodynamic cell entrapment. In the main channel, trap units are alternately arranged with suitable spacing to ensure that all cells, carried by the liquid flow into the channel, will be effectively trapped. This design aims to ensure that every simulated cell in the flow path becomes captured due to the repetitive and staggered configuration of the trap arrays. Each trap unit exclusively accommodates a single cell. In this work, human embryonic stem cells (hESCs) were used to verify the working mechanism of the proposed biochip by using simulation methods, with the referenced mechanical parameters being Young's modulus and Poisson's ratio (Kiss et al. 2011; Shin et al. 2016). The design parameters of the 3μPF device are illustrated in Table 1. Each trap unit is designed to ensure that the pillar position and the trap area are suitable to trap only a single cell while eliminating the existence of more than one cell. Since the cell diameter is 16 µm, the opening of the trap unit T_gap is a little greater, at 23 µm. When considering pillar size, bigger pillars might lead to low cell surface exposed to medium while smaller pillars could encounter the complex fabrication process. The pillar size of 5–10 µm was found to be appropriate for stem cells (He et al. 2022; Long et al. 2024) and is compatible with human embryonic stem cell (hESC) size. In this research, micropillars with diameter of 5 µm were used. Based on the hydrodynamic mechanism, the trap units are interleaved (Carlo et al. 2006); therefore, in this work, the gap between the two neighboring traps on the same row R_w is equal to a trap opening. The gap between two successive rows is required to be greater than the cell diameter so that cells can pass through the filled trap units.

Initially, the fluid traverses the channel, carrying multiple cells. Upon passing through the trap units, each cell is captured in a unit trap, leading to a gradual decrease in velocity to zero at this position. The trapping mechanism is illustrated in the inset of Fig. 1 within the trap method section. A schematic representation illustrates the hydrodynamic resistance of the flow in the proposed 3 $_\mu$PF under two cases: an empty trap unit (pre-trapping) and post-successful entrapment of a cell. When a cell is caught in a trap unit, the surrounding velocity will approach zero, the cell will tend to move in the direction of greater velocity and avoid the filled trap units. This structure, in addition to ensuring good single-cell trapping performance, can be used for long-term

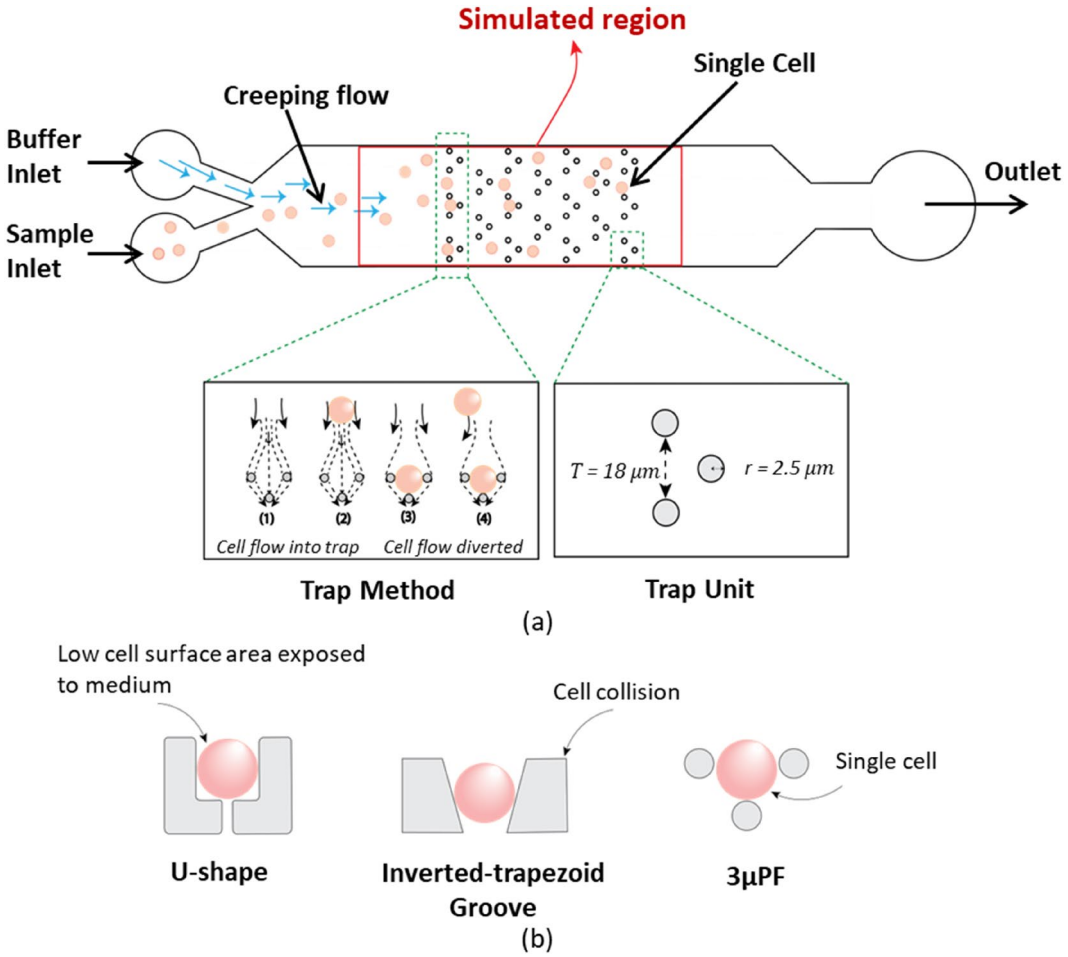

Fig. 1 (**a**) Design of the proposed microfluidic chip device. The microfluidic chip has two inlets for cell introduction and medium input, and an outlet. The single-cell is trapped based on hydrodynamic mechanism, with each trap unit designed with three micropillars; (**b**) The comparison between the proposed trap unit with two other trap units, namely U-shape and inverted-trapezoid groove

Table 1 Geometrical parameters

Name	Description	Value
L_CHIP	Chip length	360 μm
W_CHIP	Chip width	140 μm
Rs	Gap between two successive rows	18 μm
Rw	Gap between two neighboring traps on the same row	23 μm
T_gap	Trap gap	23 μm
R	Radius of the simulated cell	8 μm
r	Radius of a micropillar	2.5 μm

single-cell culture for further investigation. The micropillars in each trap unit have the advantage of micrometer size which facilitates the increase in the contact area of the cell with the culture medium or other nutrients—ensuring that the concentration of the medium inside and outside the trap is almost identical. In addition, the microfluidic chip design enables the dynamic culture of single cells, permitting continuous nutrient supply and waste removal.

3.2 Simulation setup

3.2.1 Simulation model

The 2D model of the 3μPF is illustrated in Fig. 2. In this work, numerical analysis was used to verify the mechanism of hydrodynamic trapping and the pillar-based concept. Therefore, the simulation model focuses only on the hydrodynamic trapping region. This simulation model consists of an inlet, a trapping area, and an outlet. The simulated cell was inserted into the microfluidic channel to determine the operating principle of the device. It is emphasized that in the equations governing solid mechanics and fluid-solid interaction, only the simulated cells are treated as the relevant "solid" entities while the traps are assumed to remain rigid, serving as fixed elements that enforce the no-slip boundary condition on the fluid. The physical properties of the structure, such as strength, load capacity, or thermal conductivity, are described through mathematical equations and

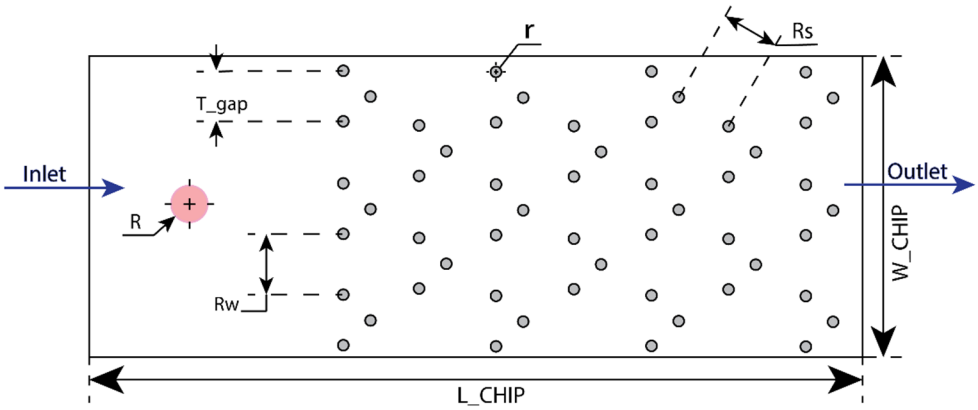

Fig. 2 2D simulation model of the proposed 3μPF structure

Table 2 Physical properties (Kiss et al. 2011; Shin et al. 2016)

Description	Value
Fluid density	1000 kg/m³
Fluid viscosity	0.001 Pa·s
PDMS density	970 kg/m³
PDMS Young's Modulus	3×10^9 Pa
PDMS Poisson's Ratio	0.49
The simulated cell density	1050 kg/m³
The simulated cell Young's Modulus	10 kPa
The simulated cell Poisson's Ratio	0.45

assigned to elements. This method simplifies the geometry and reduces the calculation without changing its hydrodynamic properties. The flow direction is characterized by the movement from regions of high pressure to those of lower pressure. A boundary condition at the outlet was initially imposed, setting the pressure value to zero. In this study, the simulation is initiated at the moment when one or more simulated cell are introduced into the channel after a time t, the simulated cell will be some distance apart from our trap arrays by the fluid flow. The physical parameters of the cells and the biochip materials are shown Table 2.

3.2.2 Boundary and initial conditions and model meshing

Computational fluid dynamics (CFD) simulations serve as a vital tool for analyzing and visualizing the effects of fluidic forces and stresses on cells, while also playing a crucial role in predicting and testing the numerous parameters that influence cell behavior in the future (Huang et al. 2010). The fluid moves from the inlet to the outlet of the channel, propelled by the pressure gradient between these two components. At the inlet, the flow is fully developed laminar characteristics, featuring a parabolic velocity profile with a mean velocity of U_0 (m/s). Meanwhile, at the outlet, the boundary condition is characterized by the absence of viscous stress and a Dirichlet condition on the pressure. Solid walls within the simulation domain, including sidewalls and fixed obstacles, are set as a no-slip wall condition, with prescribed mesh displacements for these walls set to zero. The specific boundary condition values are clearly depicted in the Fig. 3.

In FSI simulations, ensuring the mesh is compatible with both the fluid and solid domains is crucial. FSI simulations are described using the Finite Element Method (FEM) and the Arbitrary Lagrangian-Eulerian (ALE) method (Hou et al. 2012). COMSOL's ALE solver is customarily tailored for FSI simulations. It functions by iteratively updating the mesh and solving the interconnected fluid-solid equations to represent the dynamic interaction between the two domains accurately. COMSOL's ALE solver employs a segregated solver approach, wherein the fluid and solid domains are solved individually, and relevant information is exchanged between these domains at each time step to accommodate the FSI effects. Sustaining the static and undeformed state of the simulated cell mesh is crucial for upholding the fundamental assumptions essential in achieving accurate simulations of the interaction between a rigid body and a deformable fluid. This approach ensures a faithful representation of the underlying physical phenomena while optimizing computational efficiency and numerical stability. Concurrently, it enables dynamic responsiveness of the fluid domain's mesh, accommodating its deformation in response to system dynamics. This approach also facilitates mesh smoothing and accommodates dynamic simulated cell mobility during simulations, effectively capturing the system's intricate dynamics.

Additionally, mesh smoothing techniques, such as Winslow smoothing and hyperelastic smoothing, are recommended for achieving mesh quality and addressing deformation challenges (Knupp 1999) (Triantafyllidis and Aifantis 1986). Winslow smoothing serves as a well-established method to enhance mesh quality, reducing element distortions and improving overall mesh performance. This method is particularly effective in areas of the simulation domain characterized by minimal to moderate deformation. In contrast, hyperelastic smoothing demonstrates exceptional capabilities in situations where the mesh experiences

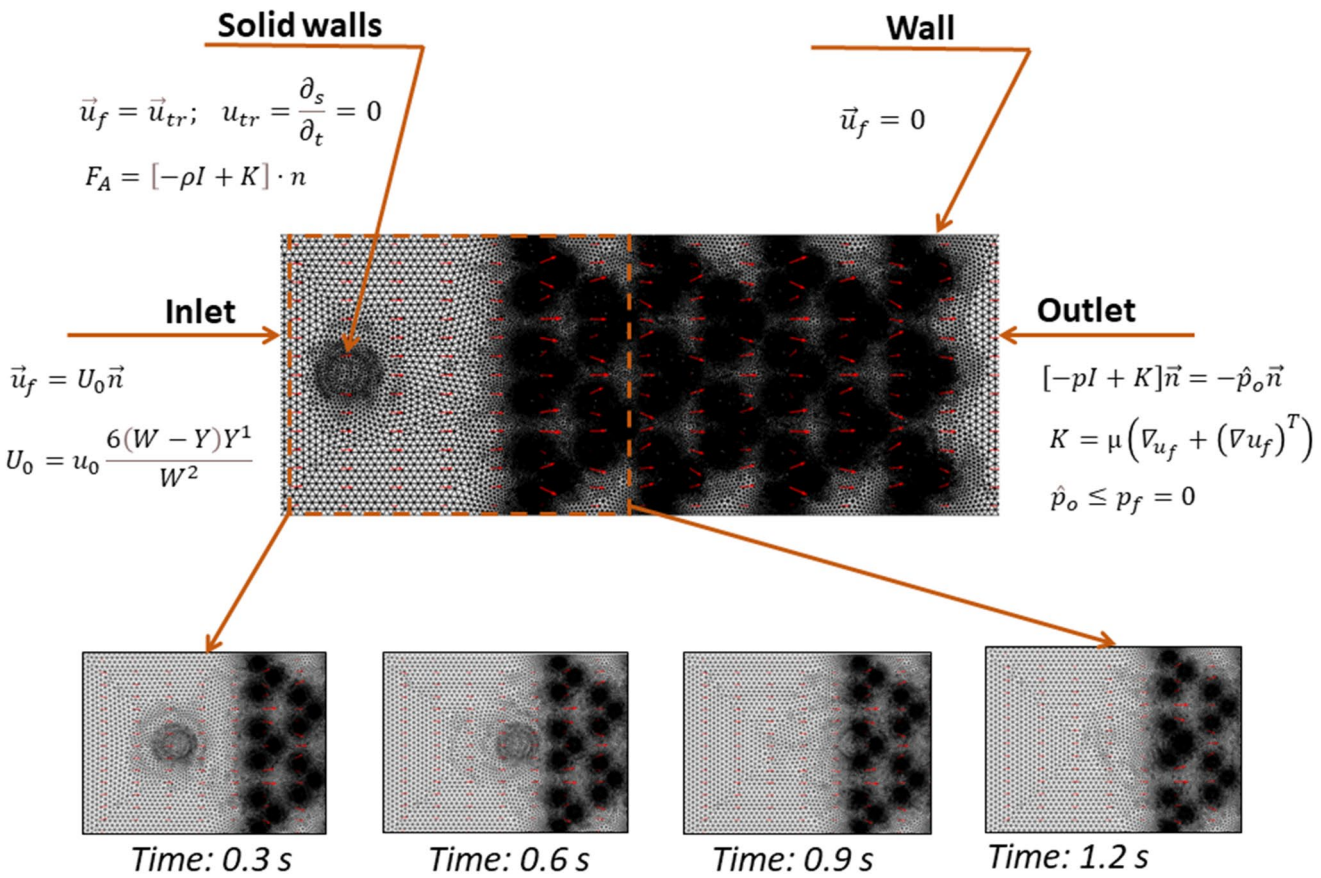

Fig. 3 Meshing model (boundary conditions and moving mesh method)

significant stretching and deformation. This technique is particularly advantageous when simulating solid particles like cells, known for their pronounced elasticity and deformation tendencies. It enables a detailed representation of complex particle behaviors under varying flow conditions. Adapting the selection of mesh smoothing methods to the unique characteristics of the simulation contributes to improved result accuracy and computational efficiency, ultimately enhancing the overall quality and effectiveness of the study. Based on the mentioned advantages, the hyperelastic smoothing method was used in this work.

Figure 3 illustrates the mesh movement in the direction of the simulated cell 's displacement at specific time points: t = 0 s, 0.3 s, 0.6 s, 0.9 s, and 1.2 s. The mesh exhibits non-uniformity, characterized by denser and smaller elements at the boundaries between the fluid and solid domains and, conversely, looser and larger elements within the fluid domain. However, it's important to note that the mesh maintains a uniform distribution around the single cell. This study opted for a finer mesh resolution to attain convergent results (Frei et al. 2017) (Anderson et al. 2004).

In scenarios where mesh deformation in the Arbitrary Lagrangian-Eulerian (ALE) method becomes substantial, such as when the simulated cell approaches the trap, the mesh quality, created and maintained by the smoothing function, can deteriorate. This may lead to elements with warped or inverted coordinates. Inverted coordinates, while not indicative of simulation failure, render results from these elements unusable in subsequent iterations. When these elements are not in the immediate region of interest, the simulation's reliability remains generally unaffected. However, a high prevalence of inverted coordinates can reduce solution accuracy and lead to convergence challenges. In this work, a solution has been implemented to solve the above problem, which involves creating a new mesh for the deformed region, allowing the solver to continue. A specified mesh quality threshold, typically less than 0.2 and within the 0 to 1 range, triggers the solver to pause and revert to a prior solution time for re-meshing. Subsequently, the simulation proceeds using the newly generated mesh, ensuring accurate and stable results despite significant mesh deformation (Storti et al. 2008; Hirt et al. 1997).

The mesh independency test was performed using four mesh types: extremely fine, finer, fine, and normal. The mesh qualities are shown in Table 3.

The single-cell trapping is directly related to the cell velocity and displacement. Therefore, the mesh independency verification is performed by calculating the cell

Table 3 Mesh qualities of four mesh types in mesh independence study

Mesh type	Maximum element size (μm)	Minimum element size (μm)	Maximum element growth rate	Curvature factor	Number of domain elements	Number of boundary elements
Extremely fine	0.905	0.0027	1.05	0.2	239,322	2916
Finer	3.78	0.054	1.1	0.25	102,217	1999
Fine	4.73	0.135	1.13	0.3	70,276	1692
Normal	6.08	0.27	1.15	0.3	62,731	1663

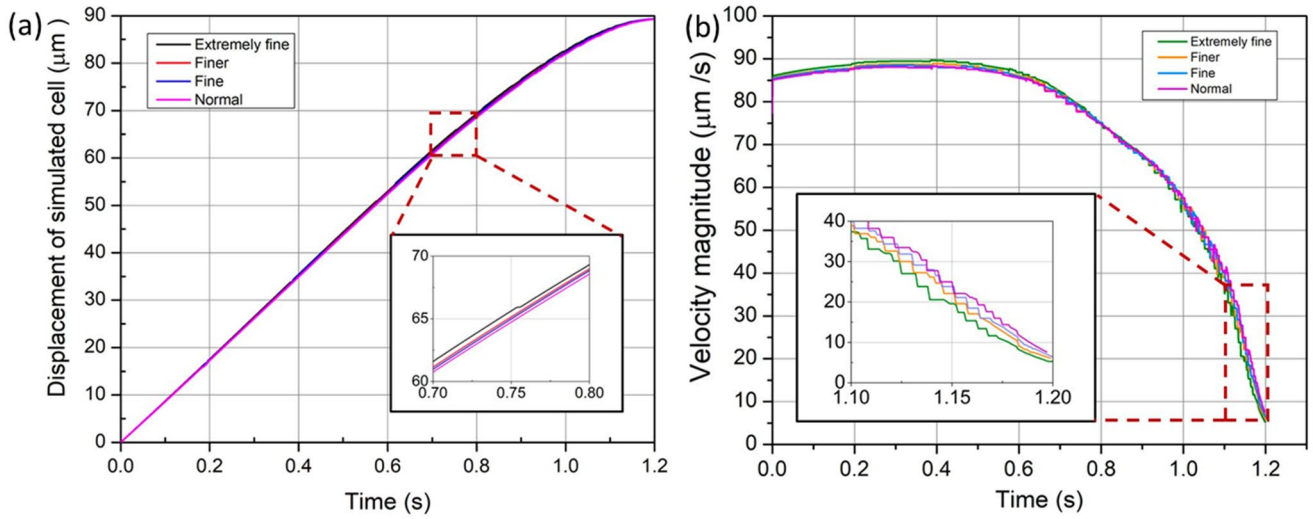

Fig. 4 Mesh independency test: (**a**) Cell displacement along the x direction versus time at different mesh scales, (**b**) Cell velocity versus time at different mesh scales

velocity and displacement over time as shown in Fig. 4. The most significant difference exists between results derived using normal mesh and extremely fine mesh. It can be seen that the differences between the cell velocity and displacement for the extremely fine and finer are quite minor. Considering the computational time, resources and to lessen the possibility of convergence fail, in this study, finer mesh was used for following analysis.

4 Simulation results and discussions

We discuss in this part the simulation results, analyze and evaluate the advantages and potentials of this device, and optimize the device geometry. The proposed device initially consists of interleaved micropillars-based trap units, each micropillar has a radius of 2.5 μm. The single cells with a radius of 8 μm follow the flow of fluid introduced into the channel. The simulation model enabled the calculation of flow velocity and pressure field. The velocity and exerted total force of the cells were calculated, the stress on and deformation of the simulated cell was also shown (Xu et al. 2013a). In addition, the cell culture potential will be analyzed by the device through the trap geometry, thanks to the low-velocity field around the trap site when cells are trapped. In order to investigate the trapping mechanism, we have implemented the situation of introducing two single cells into the channel.

4.1 Flow velocity field and simulated cell displacement

First, simulations are performed in case the input velocity of the inlet is v = 70 μm/s. The analysis of fluid velocity within both the main channel and the trap channel is conducted both prior to and following the cell trapping process. Initially, the fluid velocity in the main channel before the cell trap region is observed to be lower than that in the trap unit, as depicted in Fig. 5. However, subsequent to the entrapment of the cell within the trap unit, the flow velocity within the trap channel gradually decreases, eventually reaching approximately 6 μm/s. The low velocity profile inside the cell culture area in the proposed microfluidic chip is consistent with several recent work performing dynamic culture (Yu et al. 2017; Nocera et al. 2022; Feng et al. 2023). The fluid velocity magnitude around the trapped cell in Fig. 4 is greater than that of about 20% of the body's mass, at approximately 0.1–2 μm/s (Clementi et al. 2018). The reduction in fluid velocity around trapped cells helps decrease the stress acting on cells while still allowing nutrient delivering. The simulation study to

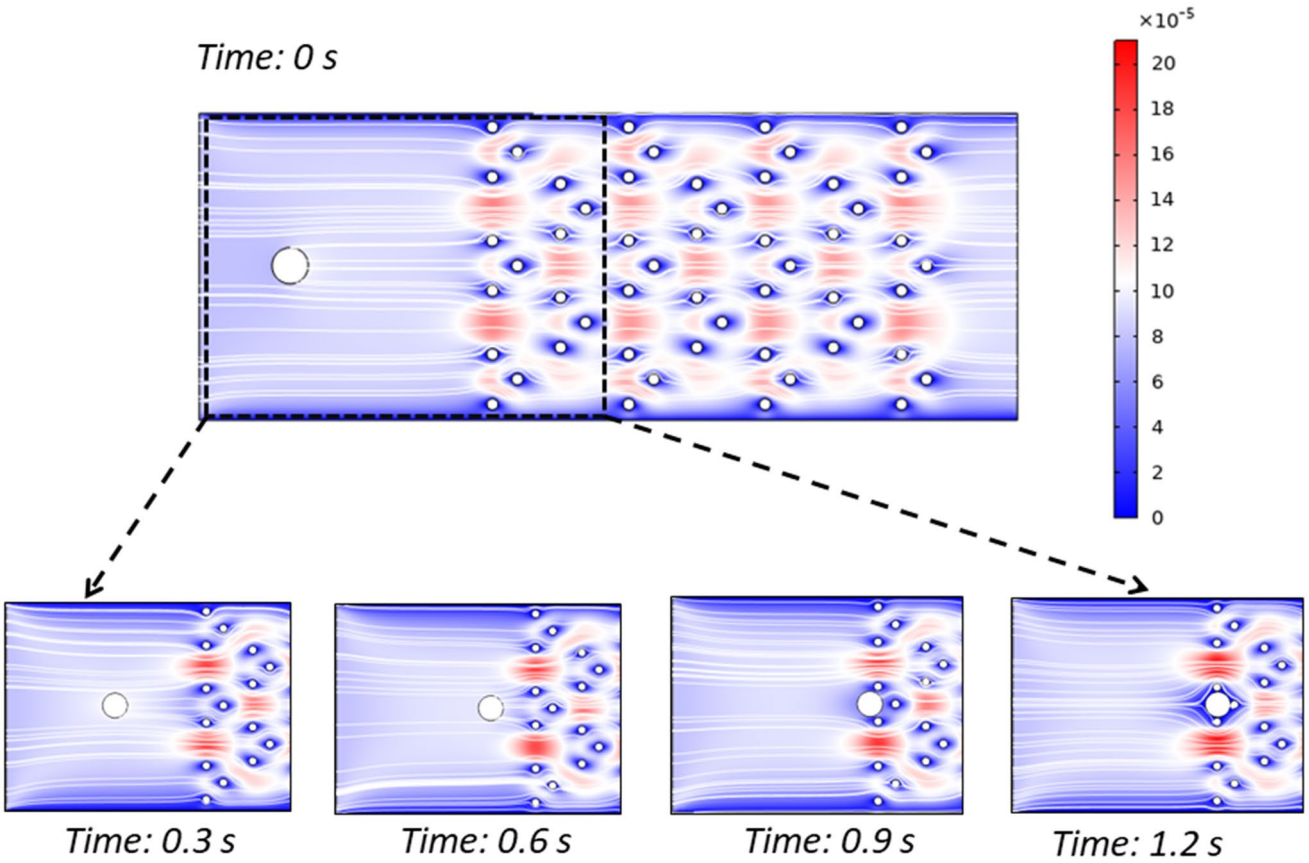

Fig. 5 Velocity magnitude distribution inside the device during the cell trapping at different time points: t = 0 s, 0.3 s, 0.6 s, 0.9 s, and 1.2 s

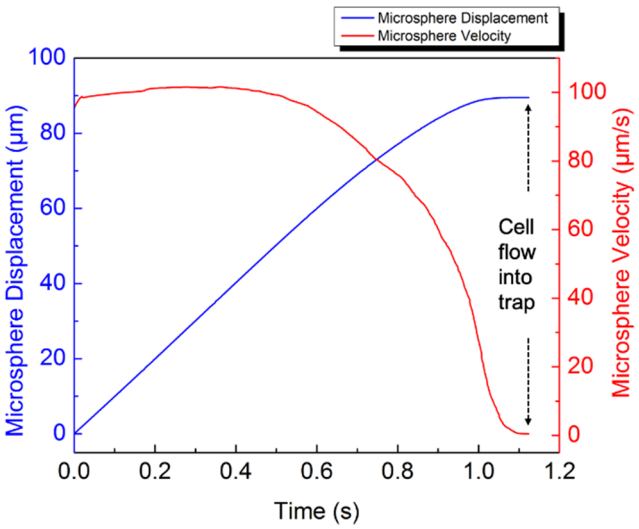

Fig. 6 Simulated cell displacement and velocity magnitude over time (until the cell was trapped)

model the transport of nutrients by means of diffusion by Fick's law and convection coupled with fluid flow shows the interaction between cells and medium.

Figure 6 illustrates the calculated flow velocity field at various time intervals, providing insights into the dynamic alterations within the system. The graphical representation in Fig. 6 includes a comparative analysis of the correlation between flow velocity and the cell displacement from the inlet. The findings illustrate a gradual reduction in fluid velocity to zero as the cell becomes entrapped within the trap unit, coinciding with an increase in the distance from its original position.

These results show that when cells are trapped in the trap unit, the contact area between the medium and the cells remains relatively large, and the flow velocity is very low. Beginning at the simulation time of 0.9s, when the cell initiates contact with the trap unit, and continuing until its full immobilization at 1.2s, there is a significant reduction in velocity, dropping from approximately 40 μm/s close to 0. This condition is particularly suitable for culturing cells within the trap under dynamic culture conditions. The low flow velocity contributes to a stable culture environment, allowing for the gradual introduction of new culture solutions and the removal of wastes. Importantly, this process can be automated, eliminating the need for manual operation, which proves advantageous during long-term culturing. Furthermore, only the flow near the simulated cell is affected by the motion of the simulated cell. When simulated cell fill a trap, flow is obstructed at the trapping site.

This observation aligns with the principle of hydrodynamic trapping, indicating that when the trapping site is empty, the trapping unit displays lower flow resistance compared to the main channel (Ahmad Khalili et al. 2016). This scenario establishes a flow pathway guiding cells toward the trap unit. Individual trapped cells obstruct the trap units, significantly decreasing liquid velocity within the trap unit. Subsequently, incoming cells are directed towards the bypass pathway, which provides a route with fewer obstructions and reduced resistance. Figure 7 clearly shows this process. The migration process of a simulated cell is considered when the opposite trap unit has been filled by another simulated cell assumed after 1.2 s in the simulation.

The simulation results are consistent with the hydrodynamic trapping theory. When a trap unit is occupied, approaching cells strategically choose to bypass the unit, opting for the path of least resistance to prevent direct entry and potential stacking. The staggered arrangement of trapping units proves effective in capturing nearly all introduced cells without overlap.

4.2 Fluid pressure and boundary load on the simulated cell

In the context of single-cell traps and microfluidic cell culture, mechanical forces generated by flow pressure fields, particularly shear stress, play a central role in influencing diverse cellular responses (Espina et al. 2023); Li et al. 2005). These responses encompass crucial aspects of cell behavior, including gene expression modulation, adhesion, migration, and signaling. Additionally, the pressure fields intricately govern microenvironment dynamics and nutrient distribution within microchannels, significantly impacting cell metabolism (Zhan et al. 2020). This microfluidic holds immense value in tissue engineering and disease modeling, faithfully replicating in vivo-like conditions.

It becomes evident that the pressure field plays an important role in cell culture. The results are calculated at specific time points t = 0 s, t = 0.3 s, t = 0.6 s, t = 0.9 s, and t = 1.2 s (Fig. 8). The findings indicate a consistently diminishing magnitude of the pressure field distribution along the channel, extending from the inlet to the outlet. When the cell is distant from the trap, it experiences the influence of flow pressure and the viscous drag present in its surrounding environment. Initially, at time t = 0, the pressure field exhibits a range of values from 0 to approximately 1.21 Pa. As the cell initiates movement, this value progressively diminishes, reaching an approximate distribution of 0 to approximately 0.75 Pa. Significantly, at time t = 1.2s, corresponding to the point when the simulated cell is positioned within the micropillar-based trap unit, there is a noticeable decrease in fluid pressure.

The simulation results demonstrate a gradual reduction in the pressure field across the entire channel. As the simulated cell consistently approached the trap unit, a progressive rise in resistance coincided with a decrease in drag force, leading to a swift decline in the velocity of the simulated cell. Upon entering the trap unit, both resistance and drag maintained a stable equilibrium, enabling the cell to move at a constant speed. Subsequently, as the resistance exceeded the drag, the simulated cell initiated a deceleration process until it eventually came to a complete stop. The results also indicate that the pressure field within this structure is lower compared to that of the inverted trapezoidal groove structure (Xu et al. 2013a). The microfluidic design with a notably reduced pressure field offers several crucial benefits (Zhu et al. 2012; Liu et al. 2013; Liang Huang, Shengtai Bian, Yinuo Cheng, Guanya Shi, Peng Liu, Xiongying Ye 2017). First and foremost, this small pressure field allows for precise control of fluid flow and the accurate positioning of cells within the microfluidic channels. This precision proves especially valuable for capturing and placing cells at specific locations and creating controlled gradients of nutrients or signaling molecules for cell culture. Additionally, the reduced pressure field minimizes shear stress on cells, which is vital for maintaining cell viability, particularly for sensitive cell types. This feature helps prevent cell damage or detachment caused by excessive mechanical forces. Moreover, the microfluidic structure's capacity to maintain a small pressure field is conducive to long-term cell culture by ensuring a stable and consistent microenvironment. This stability is crucial for extended cell culture studies. So,

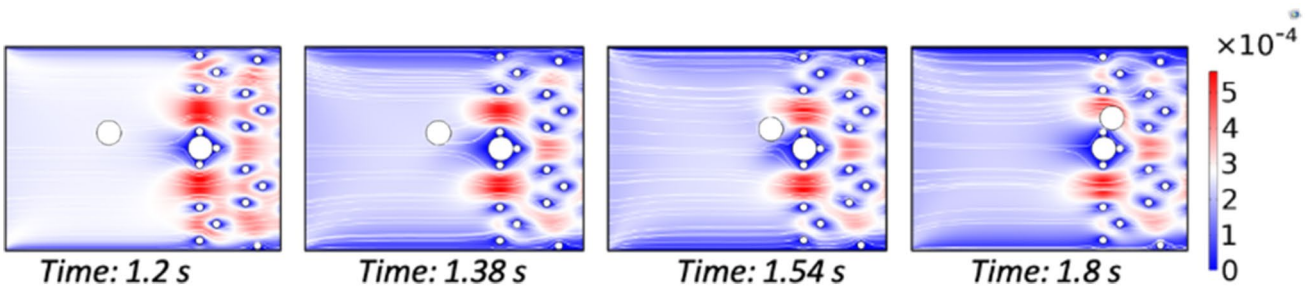

Fig. 7 Cell movement toward a filled trap unit

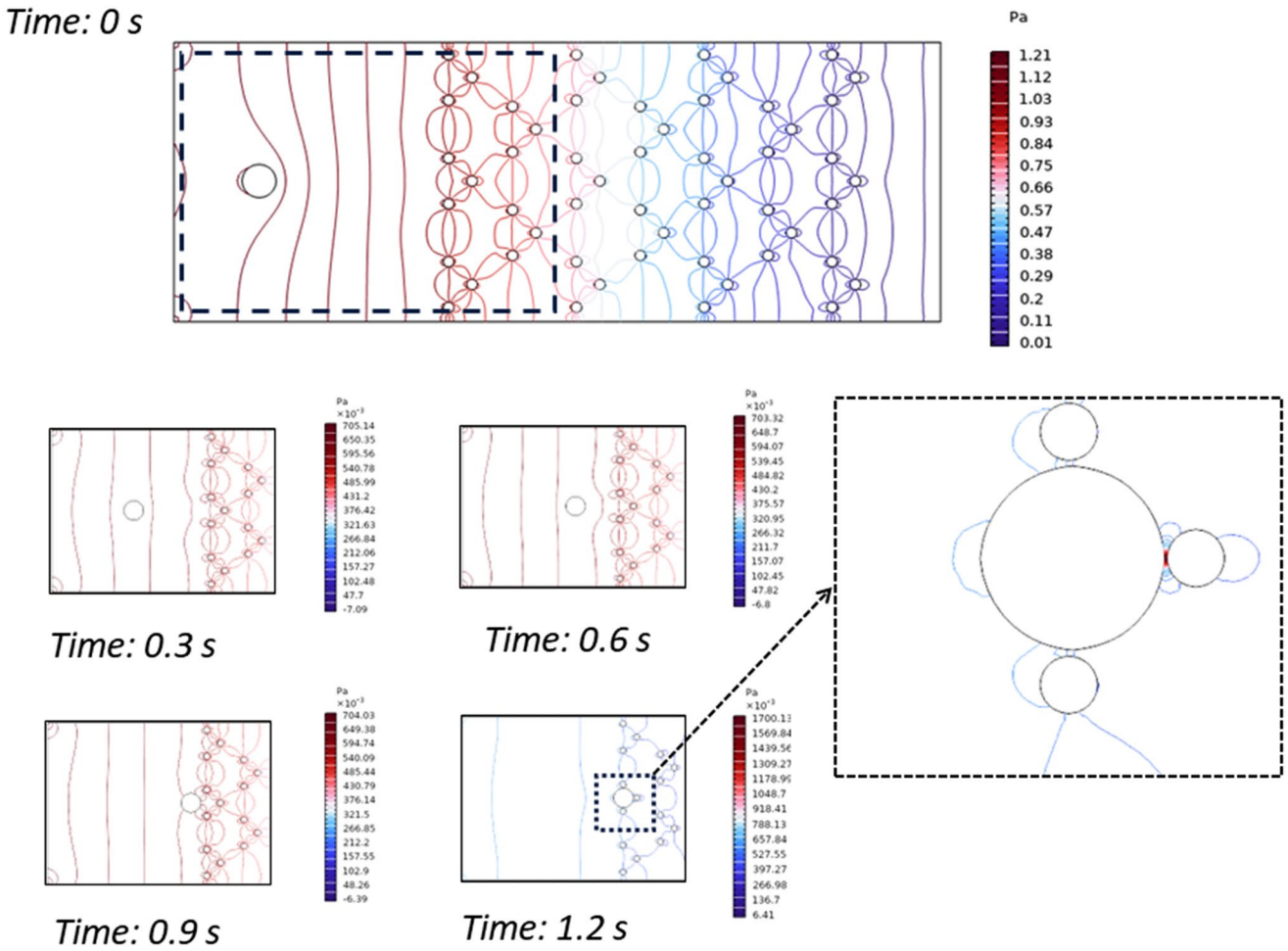

Fig. 8 Visualization of the fluid pressure field extracted during the single-cell trap simulation

this design is well-suited for single-cell investigations and applications requiring the isolation and precise positioning of individual cells, making use of the benefits of the reduced pressure field for high-precision trapping and positioning of single cells.

The relationship between fluid pressure and the total cell boundary load, encompassing both normal and tangential loads, is contingent upon the specific conditions and characteristics of the system under consideration. Within the context of fluid-structure interaction (FSI) simulations, the impact of tangential and normal loads on structures, considered here as simulated cells, due to fluid forces is a critical aspect influencing the behavior of these cell-like entities (Papadakis et al. 2022). These loads, integral components of the total force exerted by the fluid on the simulated cell surface, contribute significantly to the deformation and stress distribution within the simulated cellular structure. Tangential loads, also known as shear loads, lead to twisting or sliding deformation patterns, influenced by the geometry and material properties of the simulated cell. Normal loads, on the other hand, induce stresses perpendicular to the cell surface, affecting overall deformation, structural response, and integrity. Elevated normal loads may result in compression or tension forces, potentially causing structural failures. In this work, the calculated load value is shown in Fig. 9, highlighting the importance of understanding dynamic behavior in fluid-structure interaction scenarios.

Beginning with the normal load, it is essential to recognize that the pressure of the fluid plays a crucial role in identifying the force exerted perpendicular to the cell boundaries. This relationship adheres to Pascal's law, which stipulates that within a confined fluid at rest, alterations in pressure are uniformly transmitted in all directions. Concomitantly, the tangential load arises from shear stress induced by fluid pressure on the cell boundaries. Shear stress materializes when adjacent layers of fluid undergo sliding motion relative to each other. The magnitude of shear stress is intricately linked to fluid viscosity and the rate of deformation.

From a mathematical standpoint, the aforementioned value is computed by dividing the result of Eq. (10) by the total area unit. The findings reveal that the initial temporal load magnitude falls within the interval of 0.2–1 N/m^2. This

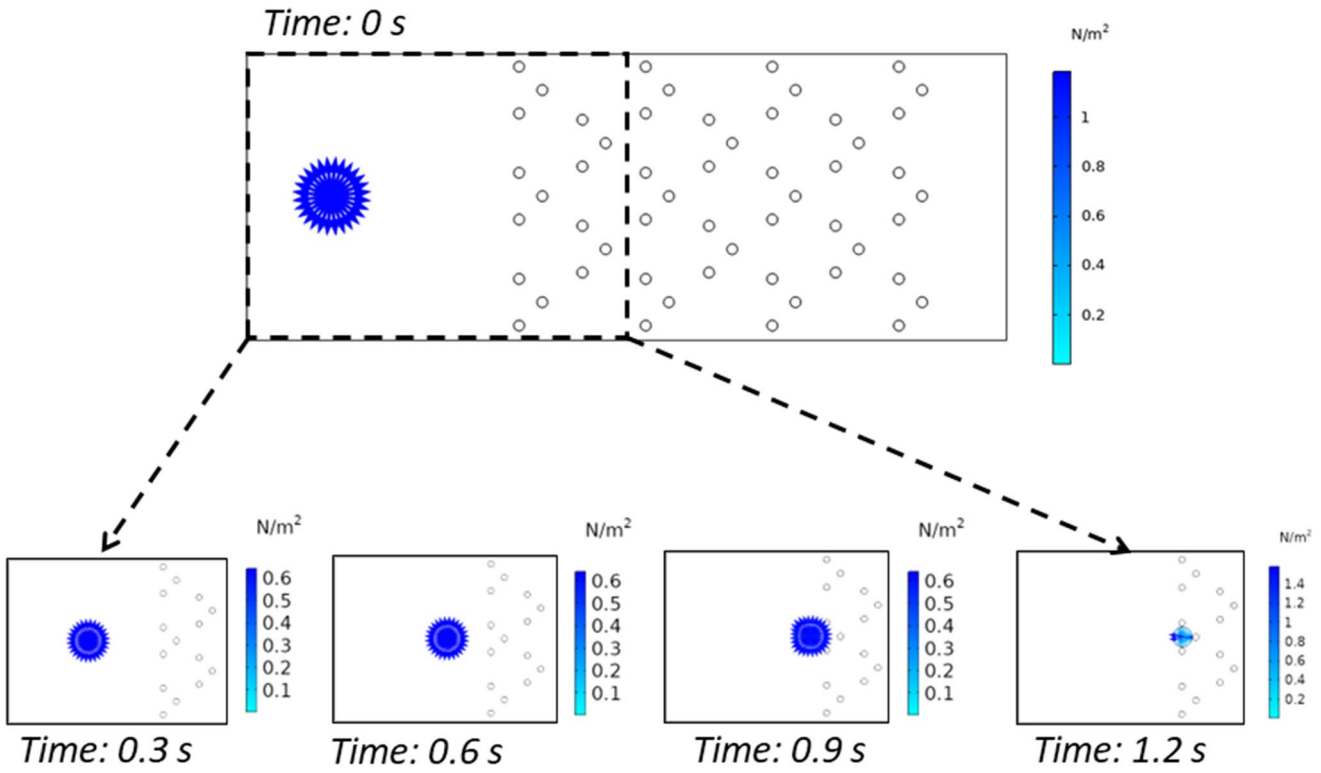

Fig. 9 Total load applied to the simulated cell

manifestation symbolizes the equilibrium influence across all spatial orientations of the the simulated cell structure. At temporal instances 0.3 s and 0.6 s, the boundary load remains in equilibrium across all orientations, albeit exhibiting a gradual reduction in magnitude, presently measuring approximately 0.2–0.6 N/m^2. Starting from 0.9 s, the value of the boundary load on the cell remains constant. However, a directional discrepancy becomes evident, with the arrow representing the outer edge of the cell (not in contact with the trap) displaying greater thickness compared to the arrow on the side of the cell facing the trap unit. Upon complete entrapment of cells within the trap unit, this value experiences a noteworthy augmentation, spanning within the range of 0–1.4 N/m^2. Nonetheless, this effect is infrequent and exhibits a pronounced bias towards one side, deviating from the direction of cell movement.

In summary, the total cell boundary load is the amalgamation of both normal and tangential loads. The specific relationship between fluid pressure and these loads hinges on the geometrical attributes of the cell, the orientation of its surfaces, and the rheological properties of the fluid, including factors such as viscosity. A comprehensive understanding of these considerations, coupled with the utilization of pertinent fluid dynamics equations, is indispensable for accurately describing this relationship within a given scenario.

4.3 Von misses stress and on the single-cell

The von Mises stress, often referred to as the von Mises yield criterion, holds significant importance in the fields of solid mechanics and materials science (Xiang et al. 2007). It serves as a valuable tool for quantifying the likelihood of yielding or failure in materials exposed to intricate stress conditions, encompassing both tensile and shear stresses (Budynas and Nisbett 2011).

Within the realm of solid-liquid interactions in microfluidics, particularly in biomedical electronics, the von Mises stress is notably pertinent. It pertains to the mechanical stresses experienced by simulated cell, here representing cells, as they traverse or interact within microfluidic channels and devices. This application is instrumental in understanding the potential mechanical deformation or injury to these sensitive biological entities. Given the inherent fragility of cells, they are highly susceptible to mechanical stresses, including shear forces encountered within microfluidic channels, which can result in deformation or damage. The assessment of von Mises stress stands as a critical determinant of whether these stresses remain within a range supportive of cellular viability (He et al. 2014), (Hartmann et al. 2006). In solid mechanics, Poisson's ratio and Young's modulus are crucial properties used in von Mises stress calculations. Poisson's ratio describes how a material responds to uniaxial stress by relating lateral contraction to axial

extension. Young's modulus represents the stiffness and capability to resist deformation of a material under axial loading. These properties collectively play a pivotal role in understanding how materials react to diverse stress conditions. The simulation results indicate that the von Mises stress impacts cells at different time intervals, specifically at t = 0 s, t = 0.3 s, t = 0.6 s, t = 0.9 s, and t = 1.2 s.

The surface results display the positions of maximum and minimum stress applied to the cell, visualized through varying levels of gradient color intensity (Fig. 10). It is evident that when the cell is not yet trapped within the trap unit, the von Mises stress is almost uniformly distributed throughout the cell and remains of relatively low magnitude. The variation between the highest and lowest stress values is very small. At the initial time, the maximum value reached 0.118 N/m^2, the minimum value reached 0.116 N/m^2, the difference is only about 0.002 N/m^2. A consistent disparity persists at subsequent temporal intervals, specifically at 0.3s and 0.6s, indicating a nearly uniform distribution of von Mises stress throughout the entire cellular surface. As the cell initiates ingress into the trapping unit, a discernible escalation in the observed discrepancy becomes apparent. Specifically, at the temporal juncture of 0.9 s, the minimum von Mises stress value attains an approximate magnitude of $0.058 N/m^2$, while the corresponding maximum value registers at 0.065 N/m^2, yielding a discernible difference of 0.007 N/m^2. Subsequently, upon complete entrapment of the cell within the trapping unit at time t = 1.2 s, the minimum von Mises stress value is recorded at 0.05 N/m^2, with the maximum value surging to 0.676 N/m^2, reflecting a ratio exceeding 13.5-fold. The rationale behind this substantial variance lies in the inherent occurrence of cell-wall collisions as cells enter the trap unit and become ensnared. Moreover, throughout the progression of cell cultivation and maturation within the confines of the trap unit, collisions with the micropillars are an inevitable aspect of the dynamic. Nonetheless, it's crucial to note that hESCs have elasticity values within the range of 0–10 kPa (1 Pa = 1 N/m^2) (Kiss et al. 2011). This implies that even when the von Mises stress values are significantly higher at the time of impact, the results demonstrate that they remain within the permissible range for cell deformation. Because the interplay between a cell's elasticity and Von Mises stress is a critical determinant of its response to external forces (Tan et al. 2012). Elasticity, quantified by the modulus of elasticity, signifies a cell's ability to endure and recover from deformation. Von Mises stress, on the other hand, measures the material's stress under external forces. Consequently, these findings indicate that the results will not lead to hESCs deformation or damage. In general, the elasticity of cells ranges from 0 to 100 kPa (Alonso and Goldmann 2003). Since the proposed device is applicable to hESCs which have elasticity values within the range of 0–10 kPa, this microfluidic structure might be suitable to various cell types.

4.4 Comparison between three- and five-micropillar trap unit

After an in-depth analysis of the trapping and static cultivation capabilities of our initial three-pillar structure, an extended survey on a modified configuration featuring five pillars. Figure 11 compares velocity field distribution between three- and five-micropillar trap unit at time t = 1.2 s

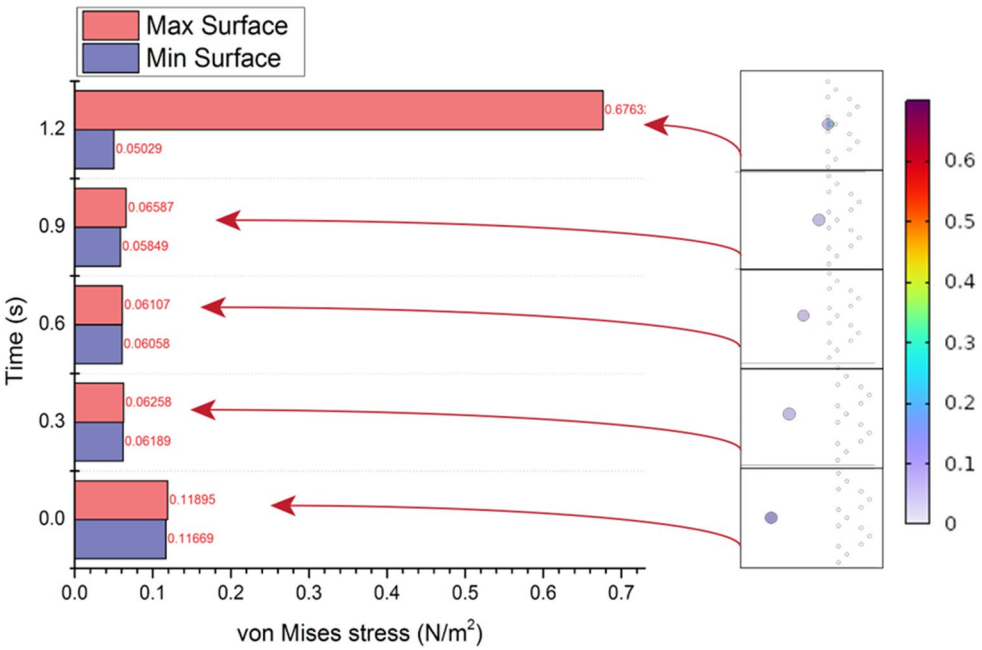

Fig. 10 Stress on the microphere during the trapping process

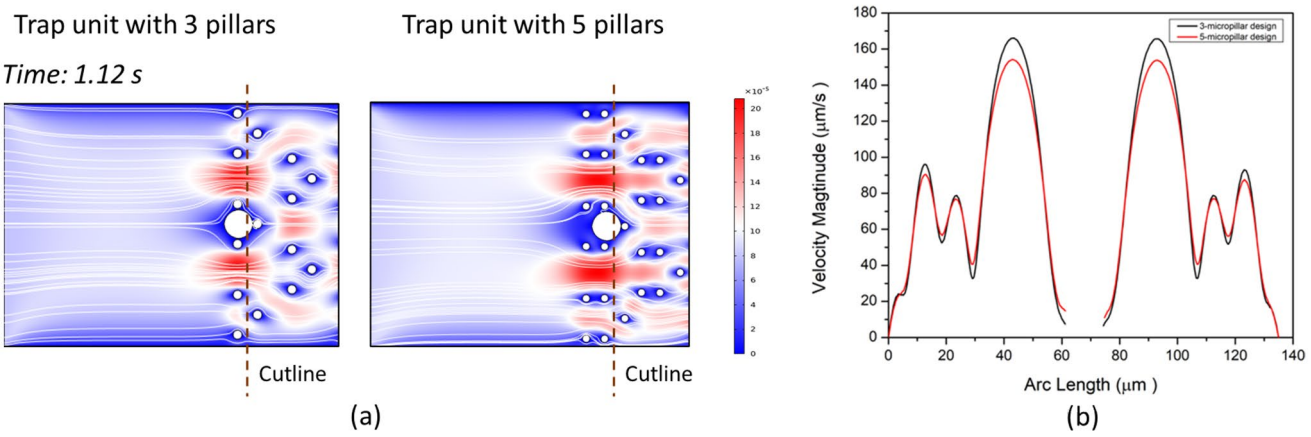

Fig. 11 (**a**) Velocity field distribution and (**b**) Velocity magnitude at the cutline of trap unit with three pillars and five pillars

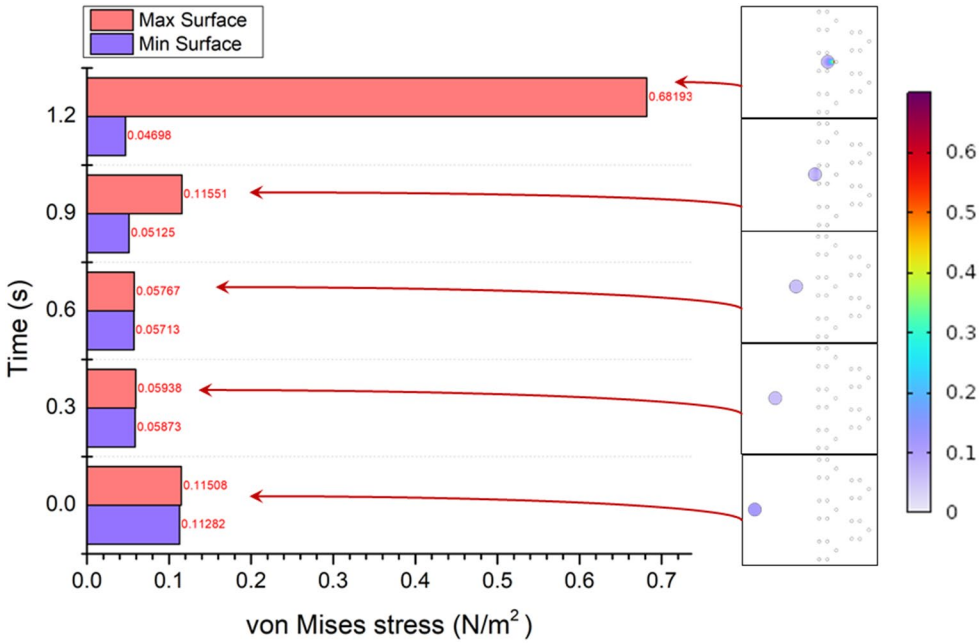

Fig. 12 Stress on the simulated cell during the trapping process of the 5-micropillar structure

(single cell captured at trap). The results revealed that the zero-velocity trapping zone within the trap region of the new structure is significantly larger, indicating an expanded area for ensuring stability in both trapping and static cell cultivation.

Figure 11 shows the velocity magnitude along the cut line at time t = 1.2 s, corresponding to fluid velocity field around the trapped cell in the trap unit. In the 5-micropillar design, the fluid velocity in the area near the cell is approximately 10 μm/s, representing a 4 μm/s increase over the velocity observed in the 3-micropillar design. This difference arises from heightened diffusion effects resulting from the greater number of pillar rows inside a trap unit, consequently resulting in a slight increase in flow rate. Figure 12 shows the von Mises stress on the cell at several time points (t = 0, 0.3, 0.6, 0.9, and 1.2 s) of the 5 micropillar structure. A comparative analysis between structures composed of 3 and 5 micropillars reveals negligible differences in the von Mises stress levels, with the maximum stress observed at approximately 0.7 Pa across both configurations. The heightened velocity levels may promote improved nutrient transportation and cell interactions within the culture medium while remaining the stress value. Additionally, the velocity region surrounding the cell within the trap structure featuring 5 micropillars remains a region of low velocity. Notably, this region exhibits a significantly broader extent compared to the configuration with 3-micropillars, contributing to the enhanced stability of the cell culture zone.

5 Conclusions

This work proposes a biochip for single-cell trapping and long-term culture using a passive trapping method based on hydrodynamic principles. The trapping unit designed with micropillars was proved to ensure high-precision single-cell entrapment, interactions between cells and culture medium, stable but dynamic culture environment. The obtained results lay strong foundations for single-cell trapping mechanism understanding as well as further design, optimization, and experiments of the proposed biochip. Our design accommodates on-site cell cultivation, offering flexibility in experimental design. Furthermore, our structure aligns with the trend of dynamic cell cultivation, enhancing utility for high-throughput studies. The micropillars within each trap unit could potentially be fabricated from polydimethylsiloxane (PDMS), an elastomer known for its biocompatibility, exceptional optical, electrical, and mechanical properties, making it well-suited for a variety of biomedical applications. Its seamless integration into automated systems positions it at the forefront of advancements in automation within cell biology. Additionally, its characteristics make it a noteworthy candidate in the development of "Organ-on-a-Chip" technology, supporting both trapping and dynamic cultivation of cells. This multifaceted design, combining simplicity with versatility, stands as a promising tool in the evolving landscape of microfluidic technology and cell biology.

Acknowledgements This work was funded by Vingroup Joint Stock Company and supported by Vingroup Innovation Foundation (VINIF) under project code VINIF.2022.DA00030. Thu Hang Nguyen was funded by the Master, PhD Scholarship Programme of Vingroup Innovation Foundation (VINIF), code VINIF.2023.TS.031.

Author contributions T.H.N, N.A.N.T, and L.D.Q conducted the literature review, ran the simulations, and analyzed the data. T.H.N, N.A.N.T, and H.B.T presented the data and wrote the main manuscript text. T.T.B, T.C.D, and L.D.Q reviewed, edited the manuscript, and supervised the project.

Data availability No datasets were generated or analysed during the current study.

Declarations

Competing interests The authors declare the following financial interests/personal relationships which may be considered as potential competing interests: Quang Loc Do report financial support was provided by Vingroup Joint Stock Company, Thu Hang Nguyen report financial support was provided by Vingroup Innovation Foundation - VinIF. If there are other authors, they declare that they have no known competing financial interests or personal relationships that could have appeared to influence the work reported in this paper.

References

Abbas SS, Nasif MS, Al-Waked R (2022) State-of-the-art numerical fluid–structure interaction methods for aortic and mitral heart valves simulations: a review. Simulation 98:3–34. https://doi.org/10.1177/00375497211023573

Ahmad Khalili A, Ahmad M, Takeuchi M et al (2016) A microfluidic device for hydrodynamic trapping and manipulation platform of a single Biological cell. Appl Sci 6:40. https://doi.org/10.3390/app6020040

Alonso JL, Goldmann WH (2003) Feeling the forces: atomic force microscopy in cell biology. Life Sci 72:2553–2560. https://doi.org/10.1016/S0024-3205(03)00165-6

Anderson RW, Elliott NS, Pember RB (2004) An arbitrary Lagrangian–Eulerian method with adaptive mesh refinement for the solution of the Euler equations. J Comput Phys 199:598–617. https://doi.org/10.1016/j.jcp.2004.02.021

Aubry G, Lee HJ, Lu H (2023) Advances in Microfluidics: technical innovations and applications in Diagnostics and therapeutics. Anal Chem 95:444–467. https://doi.org/10.1021/ACS.ANALCHEM.2C04562/ASSET/ACS.ANALCHEM.2C04562.FP.PNG_V03

Bakker B, Taudt A, Belderbos ME et al (2016) Single-cell sequencing reveals karyotype heterogeneity in murine and human malignancies. Genome Biol 17:115. https://doi.org/10.1186/s13059-016-0971-7

Bower AF (2009) Applied mechanics of solids. CRC

Budynas RG, Nisbett JK (2011) Shigley's mechanical engineering design. McGraw-Hill New York

Clementi A, Egger D, Charwat V, Kasper C (2018) Cell Culture conditions: cultivation of stem cells under dynamic conditions. Cell Eng Regen 1–33. https://doi.org/10.1007/978-3-319-37076-7_58-1

Di Carlo D, Aghdam N, Lee LP (2006) Single-cell enzyme concentrations, kinetics, and inhibition analysis using high-density hydrodynamic cell isolation arrays. Anal Chem 78:4925–4930. https://doi.org/10.1021/AC060541S/SUPPL_FILE/AC060541SSI20060425_074538.PDF

Dusny C, Grünberger A (2020) Microfluidic single-cell analysis in biotechnology: from monitoring towards understanding. Curr Opin Biotechnol 63:26–33. https://doi.org/10.1016/j.copbio.2019.11.001

Espina JA, Cordeiro MH, Milivojevic M et al (2023) Response of cells and tissues to shear stress. J Cell Sci 136. https://doi.org/10.1242/JCS.260985/329488

Feng Y, Zeng Y, Fu J et al (2023) A stand-alone microfluidic chip for long-term cell culture. Micromachines 14:207. https://doi.org/10.3390/MI14010207/S1

Frei S, Holm B, Richter T et al (eds) (2017) Fluid-structure Interaction. De Gruyter

Goldman SL, MacKay M, Afshinnekoo E et al (2019) The impact of heterogeneity on single-cell sequencing. Front Genet 10. https://doi.org/10.3389/fgene.2019.00008

Hartmann C, Mathmann K, Delgado A (2006) Mechanical stresses in cellular structures under high hydrostatic pressure. Innov Food Sci Emerg Technol 7:1–12. https://doi.org/10.1016/j.ifset.2005.06.005

He P, Liu Y, Qiao R (2014) Fluid dynamics of the droplet impact processes in cell printing. Microfluid Nanofluidics 18. https://doi.org/10.1007/s10404-014-1470-3

He Y, Yu Y, Yang Y et al (2022) Design and aligner-assisted fast fabrication of a microfluidic platform for quasi-3D cell studies on an elastic polymer. Bioact Mater 15:288–304. https://doi.org/10.1016/J.BIOACTMAT.2021.12.010

Henrik B (2008) Theoretical Microfluidics

Hirt CW, Amsden AA, Cook JL (1997) An Arbitrary Lagrangian–Eulerian Computing Method for all Flow speeds. J Comput Phys 135:203–216. https://doi.org/10.1006/jcph.1997.5702

Hou G, Wang J, Layton A (2012) Numerical methods for fluid-structure Interaction — A Review. Commun Comput Phys 12:337–377. https://doi.org/10.4208/cicp.291210.290411s

Huang M, Fan S, Xing W, Liu C (2010) Microfluidic cell culture system studies and computational fluid dynamics. Math Comput Model 52:2036–2042. https://doi.org/10.1016/j.mcm.2010.01.024

Jiang L, Korivi NS (2014) Microfluidics: technologies and applications. In: Nanolithography. Elsevier, pp 424–443

Jo MC, Liu W, Gu L et al (2015a) High-throughput analysis of yeast replicative aging using a microfluidic system. Proc Natl Acad Sci U S A 112:9364–9369. https://doi.org/10.1073/PNAS.1510328112/SUPPL_FILE/PNAS.1510328112.SM07.MP4

Jo MC, Liu W, Gu L et al (2015b) High-throughput analysis of yeast replicative aging using a microfluidic system. Proc Natl Acad Sci 112:9364–9369. https://doi.org/10.1073/pnas.1510328112

Kapałczyńska M, Kolenda T, Przybyła W et al (2016) 2D and 3D cell cultures – a comparison of different types of cancer cell cultures. Arch Med Sci. https://doi.org/10.5114/aoms.2016.63743

Kim J, Hayward RC (2012) Mimicking dynamic in vivo environments with stimuli-responsive materials for cell culture. Trends Biotechnol 30:426–439. https://doi.org/10.1016/j.tibtech.2012.04.003

Kiss R, Bock H, Pells S et al (2011) Elasticity of human embryonic stem cells as determined by Atomic Force Microscopy. J Biomech Eng 133. https://doi.org/10.1115/1.4005286

Knupp PM (1999) Winslow Smoothing on two-dimensional unstructured meshes. Eng Comput 15:263–268. https://doi.org/10.1007/s003660050021

Kuan DH, Wu CC, Su WY, Huang NT (2018) A microfluidic device for Simultaneous Extraction of Plasma, Red Blood cells, and On-Chip White Blood Cell Trapping. Sci Rep 2018 81 8:1–9. https://doi.org/10.1038/s41598-018-33738-8

Li YSJ, Haga JH, Chien S (2005) Molecular basis of the effects of shear stress on vascular endothelial cells. J Biomech 38:1949–1971. https://doi.org/10.1016/J.JBIOMECH.2004.09.030

Liang Huang SB, Cheng Y, Shi G, Liu P, Xiongying Ye WW (2017) Apture, Microfluidics cell sample preparation for analysis: advances in efficient cell enrichment and precise single cell. Biomicrofluidics. https://doi.org/10.1063/1.4975666

Liu M-C, Shih H-C, Wu J-G et al (2013) Electrofluidic pressure sensor embedded microfluidic device: a study of endothelial cells under hydrostatic pressure and shear stress combinations. Lab Chip 13:1743. https://doi.org/10.1039/c3lc41414k

Long Y, Sun Y, Jin L et al (2024) Micropillars in Biomechanics: role in guiding mesenchymal stem cells differentiation and bone regeneration. Adv Mater Interfaces 11:2300703. https://doi.org/10.1002/ADMI.202300703

Muhl L, Genové G, Leptidis S et al (2020) Single-cell analysis uncovers fibroblast heterogeneity and criteria for fibroblast and mural cell identification and discrimination. Nat Commun 11:3953. https://doi.org/10.1038/s41467-020-17740-1

Narayanamurthy V, Nagarajan S, Firus Khan AY et al (2017) Microfluidic hydrodynamic trapping for single cell analysis: mechanisms, methods and applications. Anal Methods 9:3751–3772. https://doi.org/10.1039/C7AY00656J

Nocera GM, Viscido G, Criscuolo S et al (2022) The VersaLive platform enables microfluidic mammalian cell culture for versatile applications. Commun Biol 2022 51 5:1–9. https://doi.org/10.1038/s42003-022-03976-8

Papadakis L, Karatsis E, Michalakis K, Tsouknidas A (2022) Cellular biomechanics: fluid-structure interaction or structural simulation? J Biomech 136:111084. https://doi.org/10.1016/j.jbiomech.2022.111084

Peksen M (2018) Multiphysics modelling of interactions in systems. Multiphysics Modelling. Elsevier, pp 139–159

Shin B, Gopaul D, Fienberg S, Kwon HJ (2016) Application of Eshelby's solution to Elastography for diagnosis of breast Cancer. Ultrason Imaging 38:115–136. https://doi.org/10.1177/0161734615573030

Sinha N, Yang H, Janse D et al (2022) Microfluidic chip for precise trapping of single cells and temporal analysis of signaling dynamics. Commun Eng 2022 11 1:1–12. https://doi.org/10.1038/s44172-022-00019-2

Storti MA, Nigro NM, Paz RR, Dalcín LD (2008) Dynamic boundary conditions in computational fluid dynamics. Comput Methods Appl Mech Eng 197:1219–1232. https://doi.org/10.1016/j.cma.2007.10.014

Tan Y, Kong C, Chen S et al (2012) Probing the mechanobiological properties of human embryonic stem cells in cardiac differentiation by optical tweezers. J Biomech 45:123–128. https://doi.org/10.1016/j.jbiomech.2011.09.007

Triantafyllidis N, Aifantis EC (1986) A gradient approach to localization of deformation. I. Hyperelastic materials. J Elast 16:225–237. https://doi.org/10.1007/BF00040814

Van de Sande B, Lee JS, Mutasa-Gottgens E et al (2023) Applications of single-cell RNA sequencing in drug discovery and development. Nat Rev Drug Discov 2023 226 22:496–520. https://doi.org/10.1038/s41573-023-00688-4

Wang H, Qin Q-H (2019) Mechanics of solids and structures. Methods of fundamental solutions in solid mechanics. Elsevier, pp 53–90

Wen L, Li G, Huang T et al (2022) Single-cell technologies: from research to application. Innov 3:100342. https://doi.org/10.1016/J.XINN.2022.100342

Xiang G, Pownuk A, Kosheleva O, Starks SA (2007) Von Mises Failure Criterion in Mechanics of Materials: How to Efficiently Use it Under Interval and Fuzzy Uncertainty. In: NAFIPS 2007–2007 Annual Meeting of the North American Fuzzy Information Processing Society. IEEE, pp 570–575

Xu X, Li Z, Nehorai A (2013a) Finite element simulations of hydrodynamic trapping in microfluidic particle-trap array systems. Biomicrofluidics 7:054108. https://doi.org/10.1063/1.4822030

Xu X, Sarder P, Li Z, Nehorai A (2013b) Optimization of microfluidic microsphere-trap arrays. Biomicrofluidics 7. https://doi.org/10.1063/1.4793713

Xu X, Wang J, Wu L et al (2020) Microfluidic single-cell Omics Analysis. Small 16:1903905. https://doi.org/10.1002/smll.201903905

Yin H, Marshall D (2012) Microfluidics for single cell analysis. Curr Opin Biotechnol 23:110–119. https://doi.org/10.1016/j.copbio.2011.11.002

Yu F, Deng R, Hao Tong W et al (2017) A perfusion incubator liver chip for 3D cell culture with application on chronic hepatotoxicity testing. Sci Rep 2017 71 7:1–16. https://doi.org/10.1038/s41598-017-13848-5

Zhan C, Bidkhori G, Schwarz H et al (2020) Low shear stress increases recombinant protein production and high shear stress increases apoptosis in human cells. https://doi.org/10.1016/j.isci.2020.101653. iScience 23:

Zhang H, Yang J, Sun R et al (2023) Microfluidics for nano-drug delivery systems: from fundamentals to industrialization. Acta Pharm Sin B 13:3277–3299. https://doi.org/10.1016/J.APSB.2023.01.018

Zhou W, min, Yan Yyan, Guo Q, ru et al (2021) Microfluidics applications for high-throughput single cell sequencing. J Nanobiotechnol 2021 191 19:1–21. https://doi.org/10.1186/S12951-021-01045-6

Zhu Z, Frey O, Ottoz DS et al (2012) Microfluidic single-cell cultivation chip with controllable immobilization and selective release of yeast cells. Lab Chip 12:906–915. https://doi.org/10.1039/C2LC20911J